Chinese Chemical Letters 36 (2025) 110432

Contents lists available at ScienceDirect

Chinese Chemical Letters

journal homepage: www.elsevier.com/locate/cclet

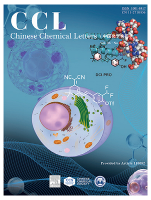

pH-responsive chiral supramolecular cysteine-Zn^{2+}-indocyanine green assemblies for triple-level chirality-specific anti-tumor efficacy

Qianyun Ye[a], Yuanyuan Liang[b], Yuhe Yuan[a], Xiaohuan Sun[a,*], Liqi Zhu[b], Xuan Wu[a], Jie Han[a,*], Rong Guo[a]

[a] School of Chemistry and Chemical Engineering, Yangzhou University, Yangzhou 225002, China
[b] College of Veterinary Medicine, Yangzhou University, Yangzhou 225002, China

ARTICLE INFO

Article history:
Received 23 April 2024
Revised 6 September 2024
Accepted 8 September 2024
Available online 12 September 2024

Keywords:
Chirality
pH-responsiveness
Photothermal therapy
Photodynamic therapy
Zn^{2+} release

ABSTRACT

Chirality, ubiquitous in living matter, plays vital roles in a series of physiological processes. The clarification of the multiple functions of chirality in bioapplications may provide innovative methodologies for engineering anti-tumor agents. Nevertheless, the related research has been rarely explored. In this study, the chiral supramolecular L/D-cysteine (Cys)-Zn^{2+}-indocyanine green (ICG) nanoparticles were constructed through the coordination interaction between L/D-Cys and Zn^{2+}, followed by the encapsulation of ICG. Experimental findings revealed that the D-Cys-Zn^{2+}-ICG exhibited 17.31 times higher binding affinity toward phospholipid-composed liposomes compared to L-Cys-Zn^{2+}-ICG. Furthermore, driven by chirality-specific interaction, a 2.07 folds greater cellular internalization of D-Cys-Zn^{2+}-ICG than L-Cys-Zn^{2+}-ICG was demonstrated. Additionally, the triple-level chirality-dependent photothermal, photodynamic and Zn^{2+} releasing anti-tumor effects of L/D Cys-Zn^{2+}-ICG *in vitro* were verified. As a result, the D-formed nanoparticles achieved 1.93 times higher anti-tumor efficiency than the L-formed ones. The triple-level chirality-mediated anti-tumor effect highlighted in this study underscores the enormous potential of chirality in biomedicine and holds substantial significance in improving cancer therapeutic efficacy.

Chirality is ubiquitous in living matter, and it is particularly interesting that chiral components in biological life exist solely in one mirror-image form [1,2]. For instance, amino acids are in L-form and sugars are in D-form [3]. The chiral preference of proteins, nucleic acids and cells through enantioselective interaction with specific enantiomers plays significant roles in metabolism, genetic information storage and transfer, cell proliferation and differentiation, toxicology and pharmacology, *etc.* [4]. As a consequence, drugs with opposite chirality can cause different or even reversed effects [5]. The thalidomide tragedy in the 1960s clearly illustrates this point. Since then, chirality has been considered a key factor to be concerned with in the perspective of bioapplication.

Supramolecular assemblies have been emerging as excellent candidates in cancer therapy [6-8]. Compared to chiral molecules, chiral nanomaterials, particularly chiral supramolecular nanomaterials, often constructed through the presence of chiral agents [9-12], can create defined chiral microenvironments throughout the whole system taking advantage of chirality transfer or chirality amplification, which could in further enhance their enantioselective interaction with chiral matters, *e.g.*, phospholipid bilayers-composed cell membranes [13-15]. Currently, taking advantage of the chirality-biased interaction with specific enantiomers, chirality-specific bioapplications, such as biosensing [16], biocatalysis [17], protein folding and misfolding [18], cellular energy metabolism [19,20], immune response [21], cell proliferation and differentiation [22], and, in particular, cytotoxicity [23,24] have been reported. For instance, Jaklenec *et al.* revealed that the D-formed cobalt oxide nanoparticle-based supraparticles exhibited greater levels of cytotoxicity than that of L-formed ones [25]. They also clarified that the chirality-specific cytotoxicity of D/L-supraparticles was attributed to their varying efficiency in cellular uptake. In addition, Liu *et al.* demonstrated that gold nanomaterials with opposite chiral morphologies showed differential cellular uptake efficiency as well, with D-formed ones exhibiting more than 30% enhanced cellular uptake compared to L-formed ones [26]. Drawing inspiration from this and similar studies, coupled with the understanding that cell apoptosis often stems from compromised intracellular organelle function [27,28], manipulating the chirality of anti-tumor nanoagents could open up novel avenues in cancer therapy. Additionally, the integration of multi-level chirality-mediated anti-tumor processes has the potential to amplify chirality-specific effects, which

---

* Corresponding authors.
E-mail addresses: xhuansun@yzu.edu.cn (X. Sun), hanjie@yzu.edu.cn (J. Han).

https://doi.org/10.1016/j.cclet.2024.110432

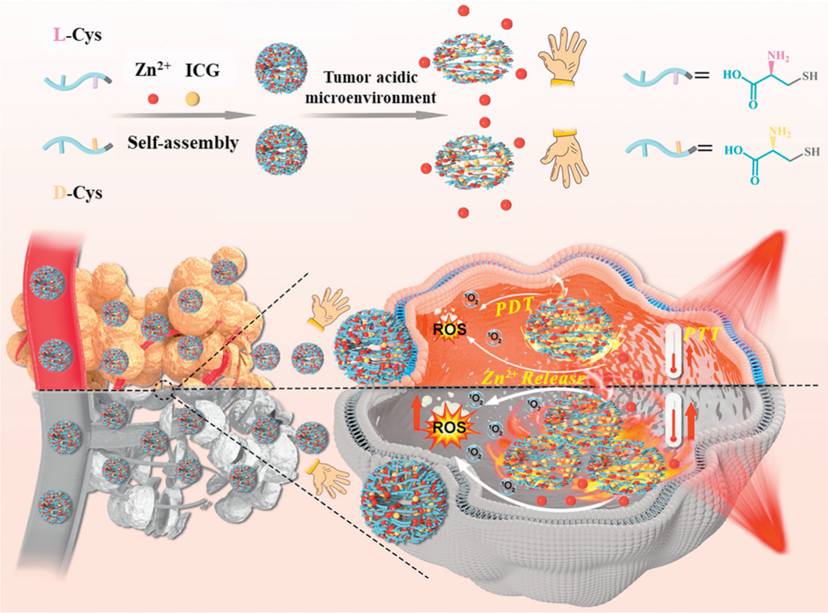

Scheme 1. Schematic illustration depicting the triple-level chirality-specific anti-tumor effects of the pH-responsive L/D-Cys-Zn^{2+}-ICG nanoparticles.

can lead to a better understanding of the importance of chirality in biotherapy. Despite its promising prospects, it is noted that there is a scarcity of related research in this area.

Cysteine (Cys) is one of the most abundant biothiols in living systems. Due to the presence of functional groups, *i.e.*, carboxylate groups, amino groups and thiol groups (-SH), Cys can bind with metal ions, *e.g.*, Zn^{2+} [29]. Since the pK_a of the -SH of Cys is ~7.4, close to normal physiological pH, the slight change of the biological microenvironment pH can vary the ionization state of -SH and thus the binding affinity between Cys and Zn^{2+} [30]. Therefore, the pH alteration in biological systems can manipulate the Zn^{2+} release behavior of Cys-Zn^{2+} related systems and initiate anti-tumor effect by increasing mitochondrial reactive oxygen species (ROS) *via* inhibiting the electron transport chain [31,32]. Considering the abovementioned facts, herein, we constructed chiral L/D-Cys-Zn^{2+} nanoparticles through the coordination between Cys and Zn^{2+}. With further encapsulation of a photothermal and photodynamic agent (indocyanine green, ICG), chiral anti-tumor agents of L/D-Cys-Zn^{2+}-ICG with the almost identical ICG encapsulation efficiency were prepared. Further results indicated that the L-Cys-Zn^{2+}-ICG and D-Cys-Zn^{2+}-ICG exhibited similar photothermal, photodynamic and pH-responsive Zn^{2+} release performance in aqueous dispersion. However, due to the higher cellular internalization efficiency, the more concentrated intracellular D-Cys-Zn^{2+}-ICG induced better photothermal and photodynamic cancer therapeutic efficacy compared to L-Cys-Zn^{2+}-ICG (Scheme 1). Moreover, the differential cellular internalization induced distinct intracellular Zn^{2+} release efficiency further amplified the chirality-specific anti-tumor efficacy. As a consequence, the D-Cys-Zn^{2+}-ICG caused 1.93 times higher anti-tumor efficiency than the L-formed ones. The simultaneous function of the triple-level chirality-specific processes well confirmed the significance of chirality in regulating cancer therapeutic efficacy.

To prepare chiral nanomaterials, a mixture of L/D-Cys and NaOH was added dropwise to $ZnCl_2$ aqueous solution. After stirring for 5 min, the mixture was washed with H_2O and the resulting precipitate of L/D-Cys-Zn^{2+} was obtained. To study the morphology of L/D-Cys-Zn^{2+} nanomaterials, the scanning electron microscopy (SEM) was carried out. From Figs. 1A and B, it is clear that both L-Cys-Zn^{2+} and D-Cys-Zn^{2+} exhibited spherical shape with an average diameter of 57 nm (Fig. S1 in Supporting information). In contrast with the nanostructures obtained by the individual L/D-Cys (Fig. S2 in Supporting information), of which were characterized as irregular nanosheets, the significant change in morphology well indicated the interaction between L/D-Cys and Zn^{2+}. The scanning transmission electron microscopy (STEM) coupled with energy dispersive X-ray spectroscopy (EDX) analysis (Figs. 1C and D) showed the homogeneous distribution of both S and Zn elements within the L/D-Cys-Zn^{2+} nanoparticles, further suggesting the interaction between L/D-Cys and Zn^{2+}. From the Fourier transform infrared spectroscopy (FTIR, Fig. 1E), the stretching vibration peak of L/D-Cys at ~2550 cm^{-1} disappeared, confirming the binding between Zn^{2+} and -SH. Moreover, the X-ray photoelectron spectroscopy (XPS) was conducted. As revealed from Fig. 1F, the signals of C, N, O, S, and Zn were clearly observed in the XPS spectra. With further analysis, the binding energies of Zn $2p_{3/2}$ and Zn $2p_{1/2}$ of L-Cys-Zn^{2+} and D-Cys-Zn^{2+} nanoparticles were identical and demonstrated to be 1021.13 eV and 1044.18 eV (Fig. 1G) respectively, indicating the Zn elements were existed in Zn^{2+} form [33]. From the S 2p spectra (Fig. 1H), compared to L/D-Cys, evident changes were occurred in the cases of L/D-Cys-Zn^{2+}. Specifically, the S $2p_{1/2}$ signals of L/D-Cys-Zn^{2+} were shifted from 163.68 eV to 163.08 eV, while that of S $2p_{3/2}$ were shifted from 162.48 eV to 161.78 eV (Fig. 1H). The changes in binding energy undoubtedly can be attributed to the altered electron density of S resulting from the coordination of -SH and Zn^{2+}.

The ultraviolet-visible (UV–vis) spectra of L/D-Cys-Zn^{2+} were further recorded, where a shift in the maximum UV–vis absorption peak from 209 nm to 225 nm (Fig. 1I), compared to L/D-Cys, was observed. These results further indicated the occurrence of the assembly between L/D-Cys-Zn^{2+} complexes. To demonstrate the driving force of the self-assembly of L/D-Cys-Zn^{2+} complex, the FTIR spectra of L/D-Cys compounds and L/D-Cys-Zn^{2+} assemblies were further analyzed. As shown in Fig. 1E, the NH stretching peaks at 3181 cm^{-1} were clearly observed in the case of L/D-Cys, while almost invisible in L/D-Cys-Zn^{2+} assemblies. In addition, the carbonyl stretching and NH deformation signals of L/D-Cys at 1579 cm^{-1} and 1527 cm^{-1} displayed distinct changes in both wavenumber and intensity compared to L/D-Cys-Zn^{2+} assemblies. Given the interaction between Zn^{2+} and Cys lies in the binding between Zn^{2+} and -SH

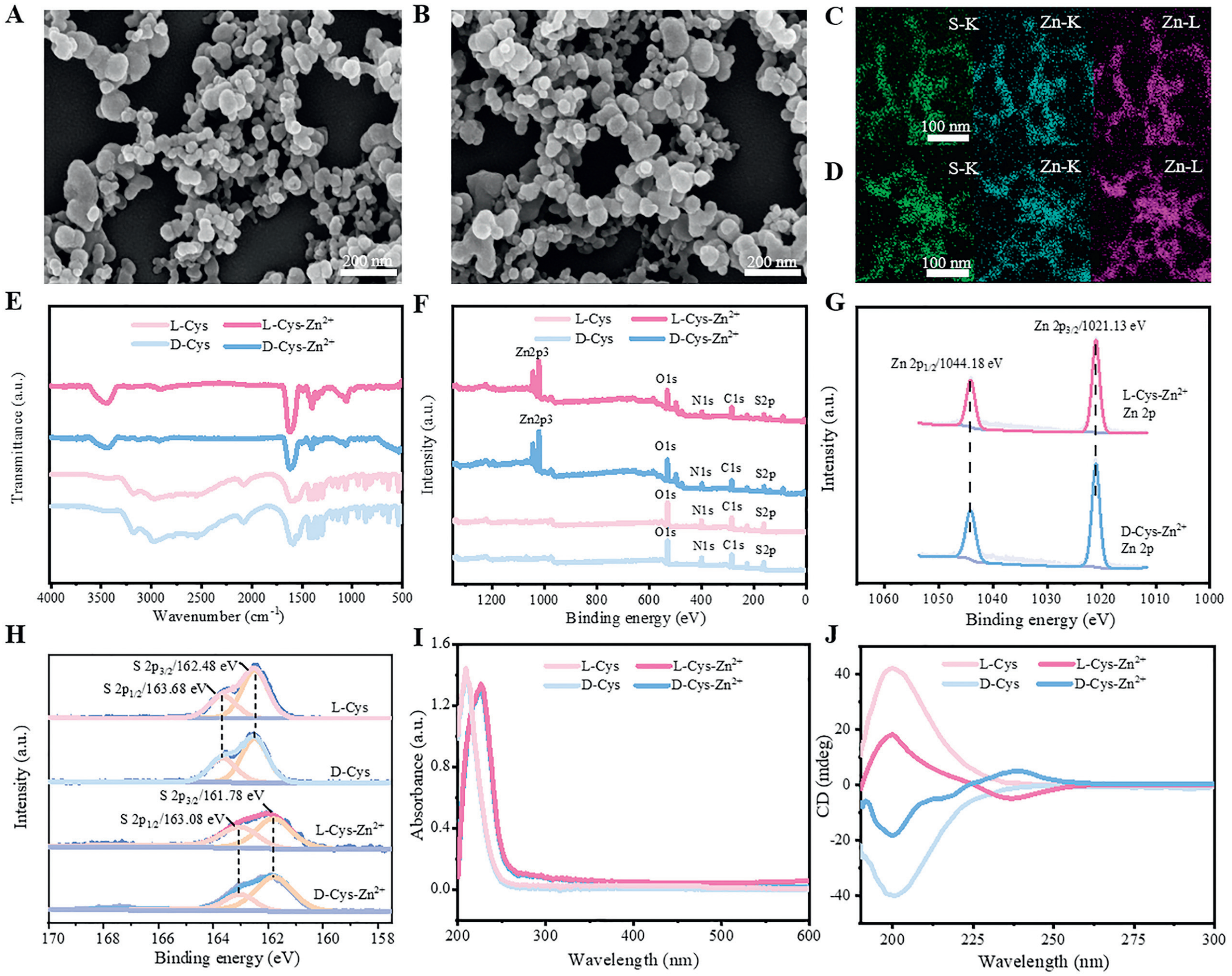

Fig. 1. SEM image of (A) L-Cys-Zn^{2+}and (B) D-Cys-Zn^{2+}. EDX mapping image of (C) L-Cys-Zn^{2+} and (D) D-Cys-Zn^{2+}. (E) FTIR spectra of L/D-Cys and L/D-Cys-Zn^{2+}. (F) XPS spectra, (G) Zn 2p XPS spectra, (H) S 2p XPS spectra, (I) UV–vis absorption spectra and (J) CD spectra of L/D-Cys and L/D-Cys-Zn^{2+}.

group, the changes of carbonyl and NH vibration peaks after self-assembly into nanoparticles showcase the intermolecular hydrogen bonding interaction between -COOH and -NH$_2$, which further attributes to the formation of L/D-Cys-Zn^{2+} supramolecular nanoparticles. To understand the chiral feature of L/D-Cys-Zn^{2+} nanoparticles, the circular dichroism (CD) spectra were investigated. As shown in Fig. 1J, the L-Cys-Zn^{2+} displayed a positive cotton effect at 200 nm and a negative cotton effect at 238 nm. While the D-Cys-Zn^{2+} showed a negative cotton effect at 200 nm and a positive cotton effect at 238 nm. The mirror-imaged CD signals of L/D-Cys-Zn^{2+} indicated their opposite chiral characteristics. In addition, with further observation, one can notice that the crossover of the CD spectra of L/D-Cys-Zn^{2+} was located at 225 nm, which is exactly overlapped with their maximum UV–vis absorption and reveals the feature of exciton-type CD spectra. These results unambiguously proved that the molecular chirality of L/D-Cys was successfully transferred to L/D-Cys-Zn^{2+} nanoparticles, resulting supramolecular chirality.

To endow the chiral L/D-Cys-Zn^{2+} nanoparticles with antitumor effect, the ICG molecules, known for photothermal and photodynamic performance [34], were encapsulated into L/D-Cys-Zn^{2+} nanoparticles. From the UV–vis spectra of L/D-Cys-Zn^{2+}-ICG (Fig. S3 in Supporting information), the characteristic UV–vis absorption peak of ICG emerged at 776 nm. Additionally, from the fluorescence spectra of L/D-Cys-Zn^{2+}-ICG, the typical fluorescent signals of ICG were observed at 814 nm (Fig. S4 in Supporting information). The above results well indicated the successful encapsulation of ICG in L/D-Cys-Zn^{2+} nanoparticles. Subsequently, according to the calibration curve of ICG (Fig. S5 in Supporting information), the encapsulation efficiency of ICG was determined to be 70.22% and 71.32% for L-Cys-Zn^{2+}-ICG and D-Cys-Zn^{2+}-ICG. Moreover, the CD spectra of L/D-Cys-Zn^{2+}-ICG were measured and no significant changes compared to L/D-Cys-Zn^{2+} were observed (Fig. S6 in Supporting information), confirming the opposite chirality was preserved in L/D-Cys-Zn^{2+}-ICG nanoparticles.

To investigate the chirality-actuated differential interaction between L/D-Cys-Zn^{2+} nanoparticles and biological systems, liposomes, with bilayer membrane structures, were synthesized using chiral lecithin through the thin film hydration method to mimic cell membranes [35]. From the confocal microscopic image, the as prepared liposomes were characterized with an average diameter of ~2 µm (Fig. S7 in Supporting information). The zeta potential measurement showed that the liposomes were featured with negative charged surfaces (Fig. S8 in Supporting information). To investigate the chirality-specific interaction between liposomes and L/D-Cys-Zn^{2+}, the surface plasmon resonance (SPR) experiments were conducted. Specifically, the liposomes were initially immobilized on a sensor chip, followed with the further addition of the

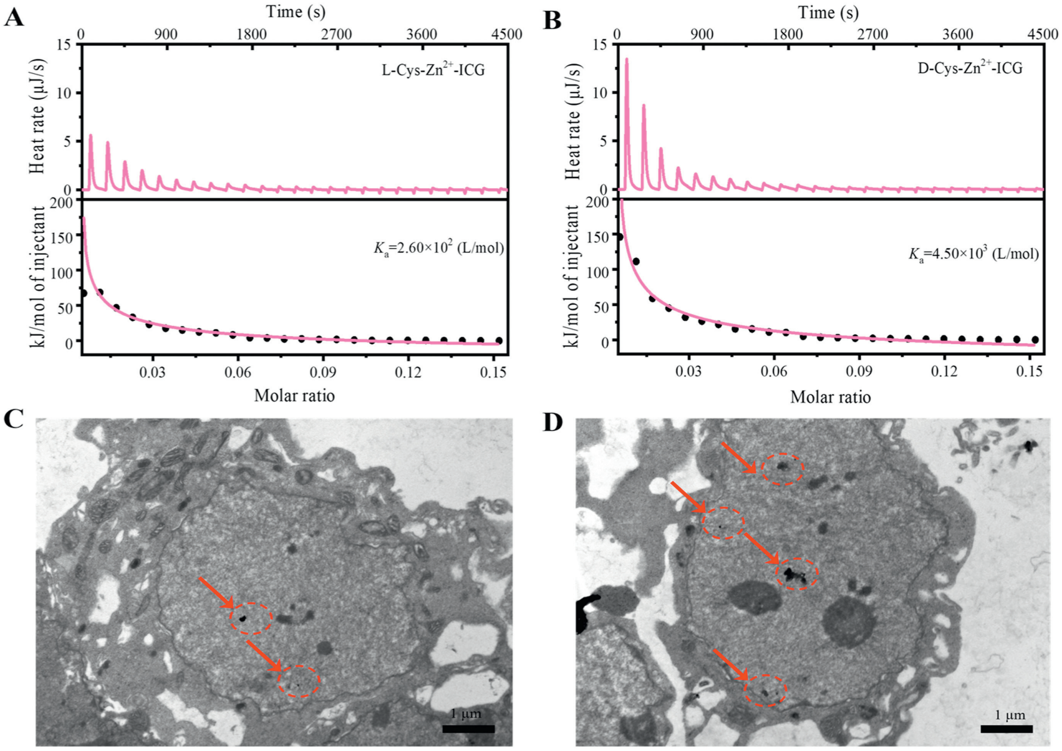

Fig. 2. ITC results for the titration of liposome dispersion into (A) L-Cys-Zn^{2+}-ICG and (B) D-Cys-Zn^{2+}-ICG. Bio-TEM images of HeLa cells after being incubated with (C) L-Cys-Zn^{2+}-ICG and (D) D-Cys-Zn^{2+}-ICG.

L/D-Cys-Zn^{2+} dispersion. As shown in Fig. S9 (Supporting information), the change of resonance angle induced by D-Cys-Zn^{2+} is evidently larger than that of L-Cys-Zn^{2+}. The calculated change ratio in resonance angle attributable to D-Cys-Zn^{2+} (the change in resonance angle before and after the addition of L/D-Cys-Zn^{2+} relative to the change in resonance angle before and after liposome immobilization, 247.0%) was approximately 2.27 times larger than that of L-Cys-Zn^{2+} (108.9%). These findings suggest a more pronounced interaction between D-Cys-Zn^{2+} and liposomes compared to L-Cys-Zn^{2+}, implying the chirality-specific interaction between L/D-Cys-Zn^{2+} and chiral liposomes. Encouraged by the above results, the chirality-dependent interaction between liposomes and L/D-Cys-Zn^{2+}-ICG was further explored using isothermal titration calorimetry (ITC) technique. By fitting the calorimetric changes during titration, the binding constants between L/D-Cys-Zn^{2+}-ICG and liposomes were demonstrated. As illustrated in Figs. 2A and B, the binding constant between D-Cys-Zn^{2+}-ICG and liposomes (4.50×10^3 L/mol) was approximately 17.31 times greater than that of L-Cys-Zn^{2+}-ICG (2.60×10^2 L/mol), which provides additional evidence for the favorable binding between D-Cys-Zn^{2+}-ICG and liposomes.

To further investigate the chirality-specific performance of L/D-Cys-Zn^{2+}-ICG nanoparticles in a biological context, these nanoparticles were separately incubated with HeLa cells for 24 h and subsequently analyzed using bio-transmission electron microscopy (Bio-TEM). As depicted in Figs. 2C and D, and Fig. S10 (Supporting information), it is noteworthy that the nanoparticles in D-form exhibited a larger cellular internalization efficiency compared to L-Cys-Zn^{2+}-ICG nanoparticles. Furthermore, the quantification of the internalized nanoparticles in cells was achieved by measuring the 2D pixels associated with L/D-Cys-Zn^{2+}-ICG nanoparticles. As illustrated in Fig. S11 (Supporting information), the statistical analysis revealed that the internalization amount of D-Cys-Zn^{2+}-ICG was 2.07 times higher than that of L-Cys-Zn^{2+}-ICG. These findings demonstrate that D-Cys-Zn^{2+}-ICG nanoparticles possess higher cellular uptake efficiency compared to L-Cys-Zn^{2+}-ICG. Given that the cell membranes are composed of chiral phospholipid bilayer, the differential cellular internalization efficiency observed can be attributed to the chirality-specific interaction between cell membranes and L/D-Cys-Zn^{2+}-ICG nanoparticles.

As the L/D-Cys-Zn^{2+}-ICG nanoparticles showed evident absorption in the NIR-I range, their photothermal performances were then investigated. Primarily, the temperature change of L/D-Cys-Zn^{2+} nanoparticles and PBS buffer solution under 808 nm laser irradiation (1.0 W/cm^2) was monitored. As shown in Fig. S12 (Supporting information), no obvious temperature increase was noticed. Nevertheless, under the identical condition, a significant temperature raise was observed for L/D-Cys-Zn^{2+}-ICG (Figs. 3A-D). In particular, the temperature change of L/D-Cys-Zn^{2+}-ICG dispersion is proportional to concentration and laser power density. Specifically, at a concentration of 1.00 mg/mL, the temperature of L/D-Cys-Zn^{2+}-ICG increased 20.4 °C within 10 min of 808 nm laser irradiation (1.0 W/cm^2). To intuitively evaluate the photothermal performance of L/D-Cys-Zn^{2+}-ICG, the infrared thermal images of L/D-Cys-Zn^{2+}-ICG dispersion upon laser irradiation at various laser power densities were collected (Figs. 3E and F) and the excellent photothermal property of L/D-Cys-Zn^{2+}-ICG was further confirmed. Moreover, it should be noted that due to the similar ICG encapsulation efficiency, the photothermal heating curves of L-Cys-Zn^{2+}-ICG and D-Cys-Zn^{2+}-ICG were nearly identical, suggesting their chirality-independent photothermal performance in aqueous dispersion. To further investigate the photothermal performance *in vitro*, the L/D-Cys-Zn^{2+}-ICG nanoparticles were separately incubated with HeLa cells for 24 h. After thorough washing to remove free L/D-Cys-Zn^{2+}-ICG nanoparticles, the HeLa cells were exposed to 808 nm laser irradiation for 4 min and the corresponding infrared thermal images were recorded. As shown in Fig. 3G, the temperature of the HeLa cells without laser irradiation was ~29 °C. After laser irra-

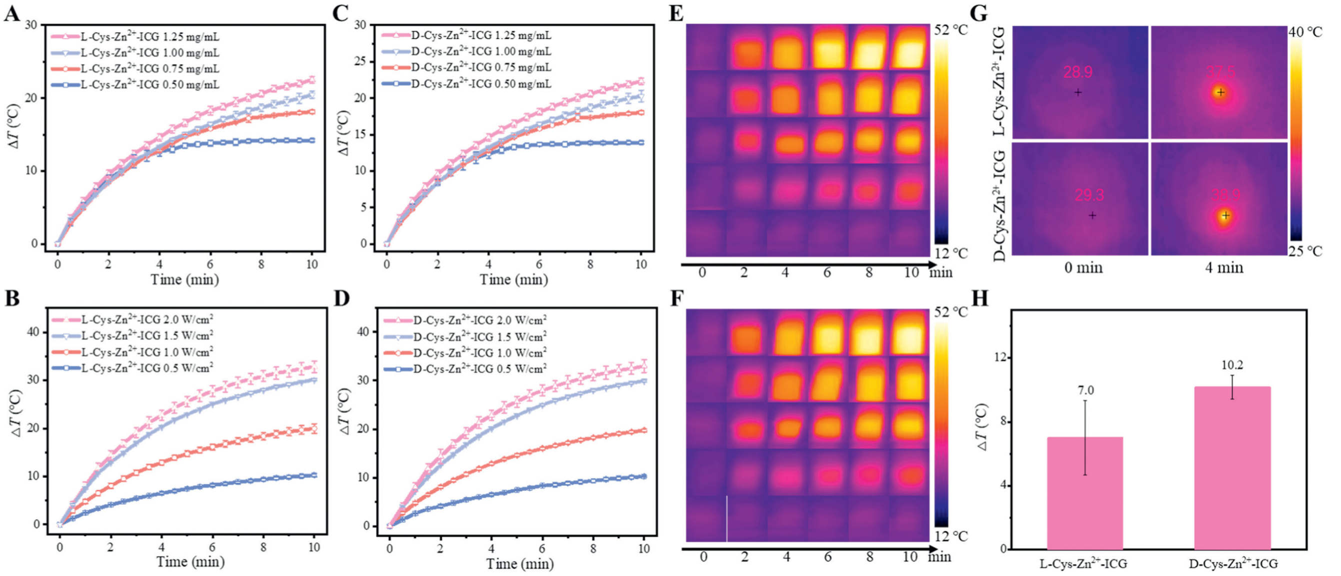

Fig. 3. Photothermal heating curves of L-Cys-Zn^{2+}-ICG (A, B) and D-Cys-Zn^{2+}-ICG (C, D) dispersions at different concentrations or different laser power densities. (E) The infrared thermal images of L-Cys-Zn^{2+}-ICG aqueous dispersions (1.00 mg/mL) upon different laser irradiation time. From top to bottom: L-Cys-Zn^{2+}-ICG (2.0 W/cm^2), L-Cys-Zn^{2+}-ICG (1.5 W/cm^2), L-Cys-Zn^{2+}-ICG (1.0 W/cm^2), L-Cys-Zn^{2+}-ICG (0.5 W/cm^2) and PBS solution (1.0 W/cm^2). (F) The infrared thermal images of D-Cys-Zn^{2+}-ICG aqueous dispersions (1.00 mg/mL) upon different laser irradiation time. From top to bottom: D-Cys-Zn^{2+}-ICG (2.0 W/cm^2), D-Cys-Zn^{2+}-ICG (1.5 W/cm^2), D-Cys-Zn^{2+}-ICG (1.0 W/cm^2), D-Cys-Zn^{2+}-ICG (0.5 W/cm^2) and PBS solution (1.0 W/cm^2). (G) The infrared thermal images of L/D -Cys-Zn^{2+}-ICG treated HeLa cells before and after 808 nm laser irradiation. (H) The quantification of the average temperature rises of L/D-Cys-Zn^{2+}-ICG treated HeLa cells after 808 nm laser irradiation. Data were presented as mean ± SD. n=3.

diation, the temperature of the L-Cys-Zn^{2+}-ICG treated HeLa cells reached 37.5 °C, while that of D-Cys-Zn^{2+}-ICG treated HeLa cells achieved 38.9 °C. With further statistical analysis (Fig. 3H), the average temperature rises of D-Cys-Zn^{2+}-ICG treated cells (10.2 °C) was 1.46 times higher than that of L-Cys-Zn^{2+}-ICG treated cells (7.0 °C). Given the almost identical photothermal performance of L/D-Cys-Zn^{2+}-ICG in aqueous dispersion, the differential photothermal behavior *in vitro* can be only ascribed to their chirality-dependent cellular internalization.

Given the photodynamic nature of ICG, the photodynamic performance of L/D-Cys-Zn^{2+}-ICG was explored using 2′,7′-dichlorodihydrofluorescein (DCFH) as a probe [36-38]. It is text knowledge that DCFH is a non-fluorescent compound. However, upon oxidation by singlet oxygen ($^1O_2$), the resulting product of 2′,7′-dichlorofluorescein (DCF) exhibits evident green fluorescence. Therefore, the monitoring of the fluorescence intensity of DCF at 524 nm can provide valuable information on $^1O_2$ generation. As revealed from Figs. 4A and B, the DCFH, DCFH + Laser, L-Cys-Zn^{2+}-

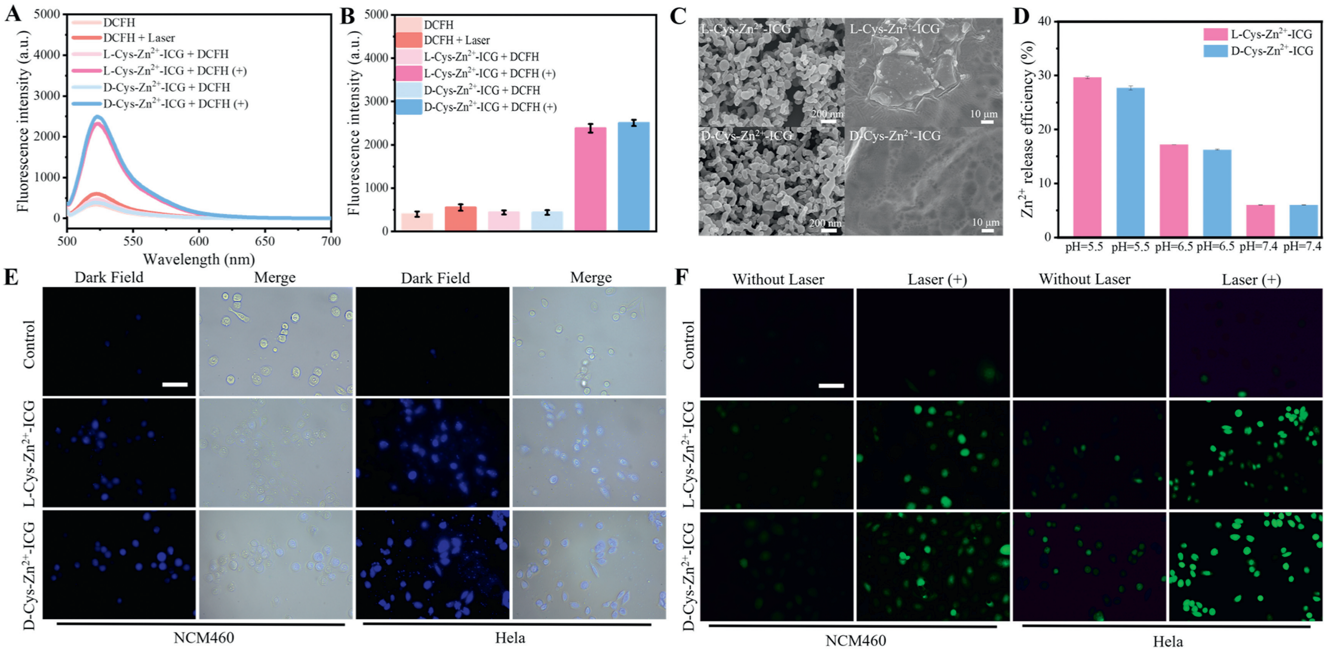

Fig. 4. (A) Fluorescence spectra and (B) fluorescence intensity (524 nm) of DCFH, L-Cys-Zn^{2+}-ICG and D-Cys-Zn^{2+}-ICG aqueous dispersions in the presence or absence of 808 nm laser irradiation. Data were presented as mean ± SD. n = 3. (C) SEM image of L-Cys-Zn^{2+}-ICG and D-Cys-Zn^{2+}-ICG at pH (left) 7.4 and (right) 6.5. (D) Zn^{2+} release efficiency of L/D-Cys-Zn^{2+}-ICG at various pH conditions. (E) Fluorescence microscopic images of zinquin ethyl ester-stained NCM460 and HeLa cells after incubation with L/D-Cys-Zn^{2+}-ICG for 4 h. Scale bar: 50 μm. (F) Fluorescence microscopic images of DCFH-DA-stained HeLa cells after various treatments. Scale bar: 50 μm. "+" represents the presence of laser irradiation.

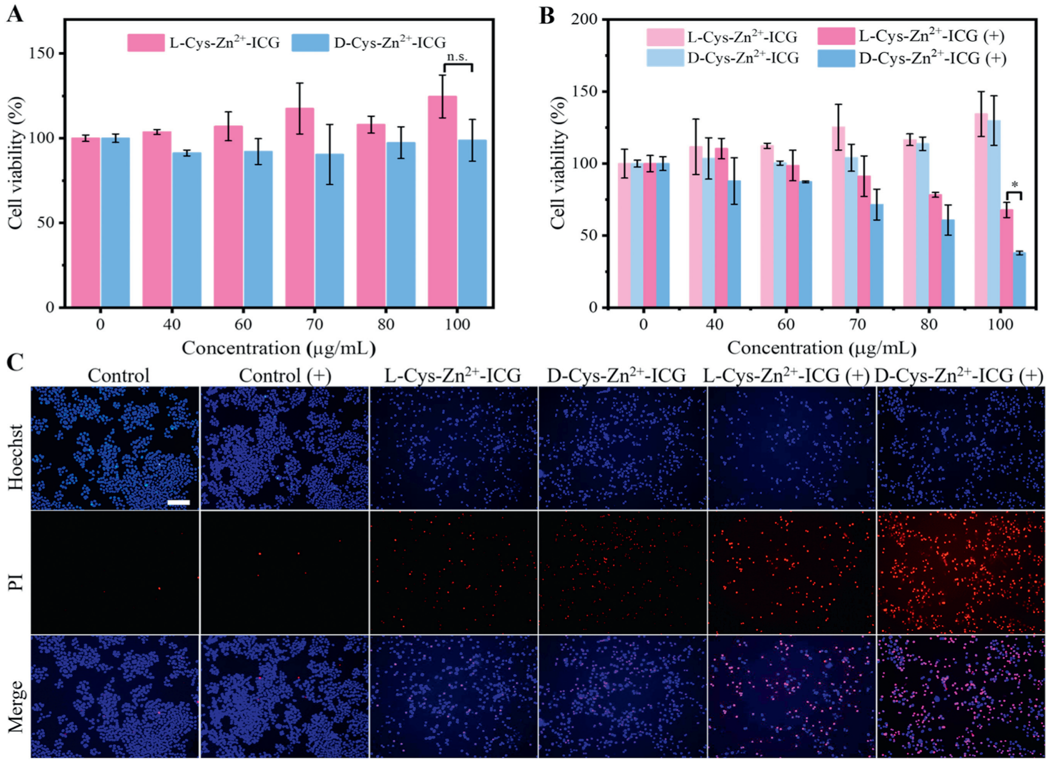

Fig. 5. Cell viability of (A) NCM-460 cells and (B) HeLa cells after being incubated with different concentrations of L/D-Cys-Zn^{2+}-ICG. (C) Fluorescence microscopic images of Hoechst/PI co-stained HeLa cells after various treatments. "+" represents laser irradiation, Scale bar: 100 μm. Data were presented as mean ± SD. $n = 3$. $^{*}P < 0.05$.

ICG + DCFH and D-Cys-Zn^{2+}-ICG + DCFH showed quite weak fluorescence. Nevertheless, upon 808 nm laser irradiation for 10 min, significant increase in fluorescence was occurred in the case of L/D-Cys-Zn^{2+}-ICG + DCFH, indicating the generation of $^{1}O_2$ and the excellent photodynamic performance of L/D-Cys-Zn^{2+}-ICG. Moreover, it is worth mentioning that, according to Figs. 4A and B, the $^{1}O_2$ generation efficiency of both L-Cys-Zn^{2+}-ICG and D-Cys-Zn^{2+}-ICG is almost identical, suggesting the chirality-independent photodynamic characteristics of L/D-Cys-Zn^{2+}-ICG in aqueous dispersions.

As discussed above, the coordination interaction between -SH and Zn^{2+} is the driving force for the construction of L/D-Cys-Zn^{2+}-ICG nanoparticles. Given the pH alteration can regulate the binding between Cys and Zn^{2+} [39], the pH responsive activity of L/D-Cys-Zn^{2+}-ICG was investigated. As depicted in Fig. 4C, the L/D-Cys-Zn^{2+}-ICG showed spherical nanostructure at neutral pH (pH 7.4). However, at pH 6.5, the initial spherical morphology of L/D-Cys-Zn^{2+}-ICG was disrupted, resulting in irregular shape. Taking in mind that the self-assembly of L/D-Cys-Zn^{2+}-ICG nanoparticles was initiated by the coordination interaction between -SH and Zn^{2+}, the alteration in morphology of L/D-Cys-Zn^{2+}-ICG at acidic condition may due to the interruption of the binding between Cys and Zn^{2+}, which may consequently induce Zn^{2+} release. To confirm the above assumption, the Zn^{2+} release of L/D-Cys-Zn^{2+}-ICG at various pH was evaluated by inductively coupled plasma-optical emission spectrometer (ICP-OES) analysis. As revealed from Fig. 4D, the L/D-Cys-Zn^{2+}-ICG showed negligible Zn^{2+} release (~5%) at pH 7.4. At pH 6.5, evident Zn^{2+} release (~16%) was observed for both L-Cys-Zn^{2+}-ICG and D-Cys-Zn^{2+}-ICG nanoparticles. When the pH was further decreased to 5.5, up to 30% of Zn^{2+} was released. The above results clearly verified the pH-responsive Zn^{2+} release performance of L/D-Cys-Zn^{2+}-ICG. Since the tumor microenvironment pH is about 6.5 and the intracellular lysosome pH is about 5.5, it is safe to say that the L/D-Cys-Zn^{2+}-ICG can undergo stimuli-responsive Zn^{2+} release in tumor tissue and initiate the anti-tumor effect by increasing mitochondrial ROS production [40].

To verify the above phenomenon in biological system, the HeLa cells were incubated with L/D-Cys-Zn^{2+}-ICG for 24 h. After thorough washing to remove free nanoparticles, the bio-TEM of the HeLa cells were carried out. As revealed from Figs. S13A and B (Supporting information), the L/D-Cys-Zn^{2+}-ICG with only irregular morphology was observed intracellularly, confirming the tumor microenvironment pH-responsive nanostructure disruption of L/D-Cys-Zn^{2+}-ICG. To further clarify the morphology alteration induced Zn^{2+} release of L/D-Cys-Zn^{2+}-ICG, the intracellular Zn^{2+} detection was conducted using zinquin ethyl ester as a probe [41]. It is known that zinquin ethyl ester itself is non-fluorescent. However, when binds to Zn^{2+}, it can generate bright blue fluorescence. As shown in Fig. 4E, when incubated with L/D-Cys-Zn^{2+}-ICG, both NCM460 cells (normal cells) and HeLa cells (tumor cells) showed obvious blue fluorescence compared to control groups. However, the fluorescence intensity produced in HeLa cells evidently surpassed that in NCM460 cells, confirming the tumor microenvironment pH-responsive Zn^{2+} release of L/D-Cys-Zn^{2+}-ICG. With further observation, in both NCM460 and HeLa cells, the D-Cys-Zn^{2+}-ICG nanoparticles always induced a greater intracellular Zn^{2+} release than that of L-Cys-Zn^{2+}-ICG, which can be attributed to their higher cellular internalization efficiency. According to the previous publication [31,42], the excessive intracellular Zn^{2+} accumulation can inhibit the mitochondrial electron transport chain and, in further, boost intracellular ROS production. Therefore, the enantioselective intracellular Zn^{2+} release of L/D-Cys-Zn^{2+}-ICG can be associated with their anti-tumor efficacy.

Given the ROS generation possibility by both Zn^{2+} release and photodynamic performance, the ROS generation capability of L/D-Cys-Zn^{2+}-ICG was evaluated using 2′,7′-dichlorodihydrofluorescein diacetate (DCFH-DA) probe. Specifically, the L/D-Cys-Zn^{2+}-ICG was separately incubated with NCM460 cells and HeLa cells. As shown

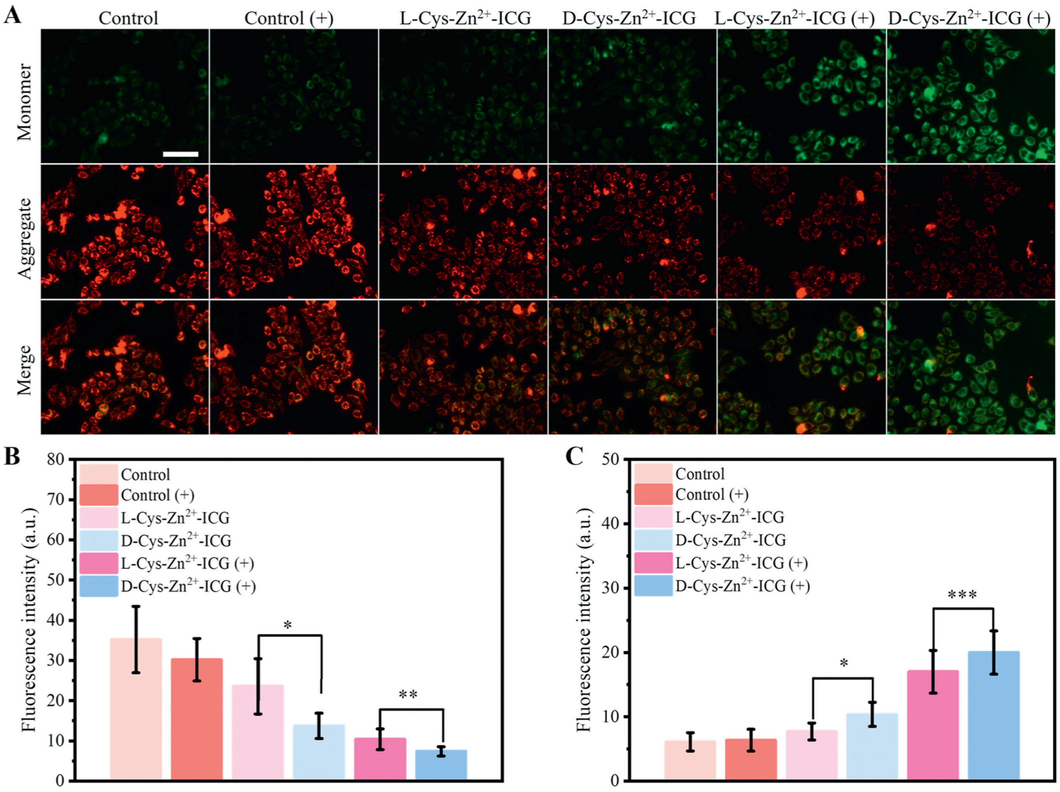

Fig. 6. (A) Fluorescence microscopic images of JC-1-stained HeLa cells after various treatments. Scale bar: 50 µm. The quantification of the fluorescence intensity of (B) the red signal and (C) the green signal of A. "+" represents laser irradiation. Data were presented as mean ± SD. n=10. $^{*}P < 0.05$, $^{**}P < 0.01$, $^{***}P < 0.001$.

in Fig. 4F, compared to the control groups, evident blue fluorescence was observed in both cases without laser irradiation, suggesting the Zn^{2+} release triggered ROS generation. While exposed to 808 nm laser irradiation, significant increase in fluorescence was detected in NCM460 cells and HeLa cells, which indicated the simultaneous function of Zn^{2+} release and the photodynamic nature of L/D-Cys-Zn^{2+}-ICG in ROS generation. Moreover, one can notice that the fluorescence intensity in the D-Cys-Zn^{2+}-ICG treated HeLa cells was consistently higher than that in the L-Cys-Zn^{2+}-ICG treated HeLa cells regardless of laser irradiation. Since the ROS generation efficiency and Zn^{2+} release efficiency of L-Cys-Zn^{2+}-ICG and D-Cys-Zn^{2+}-ICG in aqueous dispersion were demonstrated to be identical, the chirality-specific intracellular ROS generation efficiency can be only attributed to their chirality-dependent cellular internalization performance.

Given the ICG may be released along with the morphology disruption of L/D-Cys-Zn^{2+}-ICG, the L/D-Cys-Zn^{2+}-ICG nanoparticles were separately dispersed at different pH conditions. Subsequently, the supernatants were collected and the UV–vis spectra were recorded. According to the calibration curves of ICG (Fig. S14 in Supporting information), it turns out that at pH 7.4, a negligible release of ICG was observed (Fig. S15 in Supporting information). At tumor acidic pH (pH 6.5), a larger amount (~10%) of ICG was released (Fig. S15), showing the pH-responsive ICG release. The above result is in consistent with the pH-responsive Zn^{2+} release performance of L/D-Cys-Zn^{2+}-ICG. To further investigate the influence of ICG release on the photothermal performance of L/D-Cys-Zn^{2+}-ICG at tumor microenvironment pH, the heating/cooling curves were recorded at pH 6.5 upon 808 nm laser irradiation (1.0 W/cm^2). As shown in Fig. S16 (Supporting information), within four heating/cooling cycles (10 min laser irradiation followed with 10 min natural cooling), the L/D-Cys-Zn^{2+}-ICG showed negligible attenuation in photothermal performance. After four heating/cooling cycles, the temperature raised ~20 °C, which enables to initiate photothermal cancer therapy. The excellent photothermal stability of L/D-Cys-Zn^{2+}-ICG revealed the ignorable influence of low ICG release efficiency on their photothermal performance.

Encouraged by the excellent photothermal performance, photodynamic performance and Zn^{2+} release induced ROS generation capability, the anti-tumor efficacy of the as synthesized chiral nanomaterials was further investigated. Initially, the cytotoxicity of L/D-Cys-Zn^{2+} and L/D-Cys-Zn^{2+}-ICG on normal cells was conducted using the cell counting kit-8 (CCK-8) method and minimal cytotoxicity was observed in the concentration range of 0–100 µg/mL (Fig. 5A and Fig. S17A in Supporting information), demonstrating their excellent biocompatibility. While incubated with HeLa cells, without laser irradiation, no tumor inhibition effect but cell proliferation was noticed for both L/D-Cys-Zn^{2+} and L/D-Cys-Zn^{2+}-ICG (Fig. 5B and Fig. S17B in Supporting information). According to the previous reports [43], low concentration of ROS enables to stimulate cell proliferation while high concentration of ROS can induce cell death. As shown in Fig. 4F, the ROS amount produced in the absence of laser irradiation, which caused by Zn^{2+} release, is relatively low. Therefore, in this case, cell proliferation instead of cell death was observed. However, upon laser irradiation, the L/D-Cys-Zn^{2+}-ICG showed significant anti-tumor efficacy (Figs. 5B and C) due to the simultaneous function of photothermal, photodynamic and Zn^{2+} release triggered ROS generating performance. What is more, at various concentrations of L/D-Cys-Zn^{2+}-ICG, the nanoparticles in D-form consistently caused higher tumor cell death than that of L-form ones. Specifically, at the concentration of 100 µg/mL, the D-Cys-Zn^{2+}-ICG achieved 62.0% of tumor cell death under 808 nm laser irradiation, which was 1.93 folds higher than that of L-Cys-Zn^{2+}-ICG (32.2%). The above results confirmed the differential anti-tumor efficacy of L/D-Cys-Zn^{2+}-ICG, which undoubtedly can be ascribed to the triple-level chirality-specific anti-tumor effects (*i.e.*, photothermal performance, photodynamic performance and Zn^{2+} release).

To further elucidate the anti-tumor mechanism of L/D-Cys-Zn^{2+}-ICG nanoparticles, the mitochondrial membrane potential was monitored using JC-1 probe [44,45]. As depicted in Fig. 6A, compared to the control groups, the L/D-Cys-Zn^{2+}-ICG-treated HeLa cells resulted in an enhancement in green fluorescence signal in the absence of laser irradiation, indicating the decrease of mitochondrial membrane potential. As the Zn^{2+} release upon tumor microenvironment pH was already confirmed, the disruption of the mitochondrial function can be attributed to the inhibition of mitochondrial electron transport chain by the excessive Zn^{2+} accumulation. When exposed to 808 nm laser irradiation, the L/D-Cys-Zn^{2+}-ICG treated HeLa cells showed significant increase in green fluorescence signal, contributing to the synergistic effects of photothermal, photodynamic, and Zn^{2+} releasing performance. Furthermore, from Fig. 6A and the corresponding statistical analysis (Figs. 6B and C), the red to green fluorescence signal switch induced by D-Cys-Zn^{2+}-ICG was notably greater than that caused by L-Cys-Zn^{2+}-ICG regardless of laser irradiation, further demonstrating the underlying chirality-specific anti-tumor effect of L/D-Cys-Zn^{2+}-ICG. Given the mitochondrial membrane potential decrease is a hallmark event of cell apoptosis, the above results suggested the L/D-Cys-Zn^{2+}-ICG nanoparticles can trigger enantioselective tumor cell death through apoptosis pathway. Taken together, the triple-level chirality-specific anti-tumor efficacy presented in this work illustrated that chirality can be employed as a key factor for optimizing cancer therapeutic efficacy.

In this study, the triple-level chirality-specific anti-tumor efficacy was demonstrated. The L/D-Cys-Zn^{2+}-ICG nanoparticles were constructed through the coordination interaction between L/D-Cys and Zn^{2+} and further encapsulation of ICG. Our findings revealed that the L/D-Cys-Zn^{2+}-ICG exhibited chirality-mediated interaction with liposomes and cells, with D-typed nanoparticles showing stronger binding affinity and higher cellular internalization efficiency than the L-typed ones. Further studies revealed that the L/D-Cys-Zn^{2+}-ICG nanoparticles exhibited almost identical photothermal, photodynamic and tumor microenvironment pH-responsive Zn^{2+} releasing performance in aqueous dispersion. Nevertheless, driven by the chirality-specific cellular internalization, differential photothermal performance, photodynamic performance and Zn^{2+} release of L/D-Cys-Zn^{2+}-ICG were achieved *in vitro*. As a consequence, the triple-level chirality-specific effects induced higher anti-tumor efficacy of D-Cys-Zn^{2+}-ICG than L-Cys-Zn^{2+}-ICG, shedding light on the crucial role of chirality in tumor treatment.

Declaration of competing interest

The authors declare that they have no known competing financial interests or personal relationships that could have appeared to influence the work reported in this paper.

CRediT authorship contribution statement

Qianyun Ye: Visualization, Methodology, Investigation, Formal analysis, Data curation. **Yuanyuan Liang:** Methodology, Investigation, Data curation. **Yuhe Yuan:** Investigation, Data curation. **Xiaohuan Sun:** Writing – review & editing, Writing – original draft, Supervision, Methodology, Funding acquisition, Formal analysis, Conceptualization. **Liqi Zhu:** Writing – review & editing, Supervision, Methodology, Data curation. **Xuan Wu:** Writing – review & editing, Conceptualization. **Jie Han:** Writing – review & editing, Supervision, Funding acquisition, Conceptualization. **Rong Guo:** Writing – review & editing, Conceptualization.

Acknowledgments

This study was supported by the National Natural Science Foundation of China (Nos. 22002138, 22372144, 22272146, 21922202), the Chinese Postdoctoral Science Foundation (No. 2021M692714) and the Priority Academic Program Development of Jiangsu Higher Education Institutions.

Supplementary materials

Supplementary material associated with this article can be found, in the online version, at doi:10.1016/j.cclet.2024.110432.

References

[1] S. Huang, H. Yu, Q. Li, Adv. Sci. 8 (2021) 2002132.
[2] K. Hou, J. Zhao, H. Wang, et al., Nat. Commun. 11 (2020) 4790.
[3] D.A. Nicholson, A. Sengupta, D.J. Nesbitt, J. Phys. Chem. B 124 (2020) 11561–11572.
[4] Y. Ma, L. Shi, H. Yue, X. Gao, Colloids Surf. B: Biointerfaces 195 (2020) 111268.
[5] P. Chen, P.P. Lv, C.S. Guo, et al., Chin. Chem. Lett. 34 (2023) 108041.
[6] Y. Ding, C. Wang, B. Lu, Y. Yao, Front. Chem. 9 (2021) 775436.
[7] Y. Wang, H. Zhong, J. Yang, Y. Yao, L. Li, Chin. Chem. Lett. 34 (2023) 108452.
[8] Y. Zhang, Y. Wang, T. Chen, et al., Chem. Commun. 59 (2023) 8266–8269.
[9] C.Q. Zhou, Y.Y. Ren, J. Han, et al., J. Am. Chem. Soc. 140 (2018) 9417–9425.
[10] T. Tian, D. Wei, L.L. Ge, et al., J. Colloid Interface Sci. 601 (2021) 746–757.
[11] B.B. Xu, J. Ye, Y. Yuan, W.L. Duan, ACS Catal. 8 (2018) 11735–11740.
[12] W.Y. Ma, B.L. Wang, Y.G. Yang, J.Y. Li, Chin. Chem. Lett. 32 (2021) 3916–3920.
[13] X. Sun, Q. Ye, Y. Liang, et al., J. Colloid Interface Sci. 657 (2024) 993–1002.
[14] J. Zhou, J. Gu, X. Sun, et al., Adv. Sci. 11 (2024) 2308493.
[15] P.L. Gao, S. Chen, S. Liu, et al., ACS Appl. Mater. Interfaces 13 (2021) 56456–56464.
[16] C.L. Hao, A.H. Qu, L.G. Xu, et al., J. Am. Chem. Soc. 141 (2019) 1091–1099.
[17] G.Y. Yuan, Z. Xi, C. Wang, et al., Acta Phys. Chim. Sin. 39 (2023) 2212061.
[18] H. Zhang, C. Hao, A. Qu, et al., Angew. Chem. Int. Ed. 59 (2020) 7131–7138.
[19] F. Li, Y. Li, X. Yang, et al., Angew. Chem. Int. Ed. 57 (2018) 2377–2382.
[20] B. Chen, L. Song, Y. Yuan, et al., ACS Appl. Mater. Interfaces 15 (2023) 651–661.
[21] L. Xu, X. Wang, W. Wang, et al., Nature 601 (2022) 366–373.
[22] X. Dou, N. Mehwish, C. Zhao, et al., Acc. Chem. Res. 53 (2020) 852–862.
[23] D. Lovison, D. Alessi, L. Allegri, et al., Chem. Eur. J. 28 (2022) e202200200.
[24] C.L. Wang, X. Wang, D.D. Wang, et al., Chin. Chem. Lett. 34 (2023) 107332.
[25] J. Yeom, P.P.G. Guimaraes, H.M. Ahn, et al., Adv. Mater. 32 (2020) 1903878.
[26] N.N. Zhang, H.R. Sun, S. Liu, et al., CCS Chem. 4 (2022) 660–670.
[27] Y. Zhang, F. Wang, C. Liu, et al., ACS Nano 12 (2018) 651–661.
[28] Y. Teng, M. Li, X. Huang, J. Ren, ACS Appl. Bio. Mater. 3 (2020) 5020–5029.
[29] Q. Meng, R. Zhao, P. Cao, et al., Chem. Eng. J. 447 (2022) 137471.
[30] N.J. Pace, E. Weerapana, Biomolecules 4 (2014) 419–434.
[31] Q.M. Ke, P. Jing, Y.H. Wan, et al., J. Colloid Interface Sci. 654 (2024) 224–234.
[32] W.Q. Ding, H.J. Yu, S.E. Lind, Cancer Lett. 271 (2008) 251–259.
[33] Q. Cui, Y. Zhao, K. Qi, Y. Yan, J. Taiwan Inst. Chem. Eng. 142 (2023) 104679.
[34] W. Li, H. Zhang, X. Guo, et al., ACS Appl. Mater. Interfaces 9 (2017) 3354–3367.
[35] C.E. Smith, A. Shkumatov, S.G. Withers, et al., ACS Nano 7 (2013) 9599–9610.
[36] Q. Zhang, T. Zhuang, X. Sun, et al., J. Colloid Interface Sci. 665 (2024) 1–9.
[37] Z.L. Xu, J. Chen, Y.A. Li, et al., J. Colloid Interface Sci. 628 (2022) 1033–1043.
[38] S. Wang, J.W. Zhang, W. Li, et al., Carbohydr. Polym. 296 (2022) 119940.
[39] L.S. Lin, J.F. Wang, J. Song, et al., Theranostics 9 (2019) 7200–7209.
[40] X.X. Fan, C.F. Ren, K.K. Ning, et al., ACS Appl. Mater. Interfaces 15 (2023) 58251–58259.
[41] Y.P. Jiang, K. Shao, F.L. Zhang, et al., Aggregate 4 (2023) e321.
[42] F.L. Zhao, A. Gao, Q. Liao, et al., Adv. Funct. Mater. (2024) 2311812.
[43] M. Yang, N.B. Nazhat, X. Jiang, et al., Br. J. Haematol. 95 (2003) 339–344.
[44] M.M. He, R. Wang, R.F. Zhang, et al., Adv. Funct. Mater. 33 (2023) 2300780.
[45] J.X. Lu, W.J. Wang, Z. Xu, et al., J. Colloid Interface Sci. 633 (2023) 657–667.